



Published in final edited form as:

Comput Med Imaging Graph. 2015 October ; 45: 63–74. doi:10.1016/j.compmedimag.2015.07.005.

A Bayesian Approach to Distinguishing Interdigitated Tongue Muscles from Limited Diffusion Magnetic Resonance Imaging

Chuyang Ye^{1,2,*}, Emi Murano³, Maureen Stone⁴, and Jerry L. Prince²

¹Brainnetome Center, Institute of Automation, Chinese Academy of Sciences, Beijing, China

²Department of Electrical and Computer Engineering, Johns Hopkins University, Baltimore, MD, USA

³Department of Radiology and Radiological Sciences, Johns Hopkins University School of Medicine, Baltimore, MD, USA

⁴Department of Neural and Pain Sciences, University of Maryland School of Dentistry, Baltimore, MD, USA

Abstract

The tongue is a critical organ for a variety of functions, including swallowing, respiration, and speech. It contains intrinsic and extrinsic muscles that play an important role in changing its shape and position. Diffusion tensor imaging (DTI) has been used to reconstruct tongue muscle fiber tracts. However, previous studies have been unable to reconstruct the crossing fibers that occur where the tongue muscles interdigitate, which is a large percentage of the tongue volume. To resolve crossing fibers, multi-tensor models on DTI and more advanced imaging modalities, such as high angular resolution diffusion imaging (HARDI) and diffusion spectrum imaging (DSI), have been proposed. However, because of the involuntary nature of swallowing, there is insufficient time to acquire a sufficient number of diffusion gradient directions to resolve crossing fibers while the *in vivo* tongue is in a fixed position. In this work, we address the challenge of distinguishing interdigitated tongue muscles from limited diffusion magnetic resonance imaging by using a multi-tensor model with a fixed tensor basis and incorporating prior directional knowledge. The prior directional knowledge provides information on likely fiber directions at each voxel, and is computed with anatomical knowledge of tongue muscles. The fiber directions are estimated within a maximum a posteriori (MAP) framework, and the resulting objective function is solved using a noise-aware weighted ℓ_1 -norm minimization algorithm. Experiments were performed on a digital crossing phantom and *in vivo* tongue diffusion data including three control subjects and four patients with glossectomies. On the digital phantom, effects of parameters, noise, and prior direction accuracy were studied, and parameter settings for real data were determined. The results on the *in vivo* data demonstrate that the proposed method is able to resolve inter-digitated tongue muscles with limited gradient directions. The distributions of the

*Address: Intelligence Building 504, 95 Zhongguancun East Road, Beijing, China, 100190. Telephone: +86-134-6632-2392, chuyang.ye@nlpr.ia.ac.cn.

Publisher's Disclaimer: This is a PDF file of an unedited manuscript that has been accepted for publication. As a service to our customers we are providing this early version of the manuscript. The manuscript will undergo copyediting, typesetting, and review of the resulting proof before it is published in its final citable form. Please note that during the production process errors may be discovered which could affect the content, and all legal disclaimers that apply to the journal pertain.

computed fiber directions in both the controls and the patients were also compared, suggesting a potential clinical use for this imaging and image analysis methodology.

Keywords

Diffusion magnetic resonance imaging; limited gradient directions; sparse reconstruction; prior directional knowledge; interdigitated tongue muscles

1. Introduction

The tongue is a critical organ for a variety of functions, including swallowing, respiration, and speech [1, 2]. It contains intrinsic and extrinsic muscles that play an important role in changing its shape and position [3]. Tongue muscles have been studied using diffusion tensor imaging (DTI) [4–9], which provides a noninvasive tool for investigating fiber tracts by imaging the anisotropy of water diffusion [10]. For example, in Gaige et al. [5], based on diffusion tensors, the technique of fiber tracking [10–13] was used to reconstruct 3D curves representing key muscle fibers and visualize the tongue anatomy. In Felton et al. [6], muscle fibers were studied together with strain rate to demonstrate the relationship between fiber organization and tissue deformation during swallowing. Using DTI, studies on the influence of interventions on the tongue muscles have also been performed. In Shinagawa et al. [8] and Shinagawa et al. [9], preliminary studies were carried out to track the deformed muscle fibers in patients with oral appliances. In Murano et al. [7], tongue muscle fibers were tracked for a patient after the glossectomy and compared with a control subject.

These studies [5–9] all used DTI-based fiber tracking [11, 13]. However, many of the tongue muscles interdigitate, and it is well known that DTI cannot represent crossing fiber directions [14]. Thus, using the tensor model is insufficient for reconstructing interdigitated tongue muscles. For example, the transverse muscle interdigitates with the genioglossus, and DTI fails to reconstruct the transverse muscle. Figure 1(a) gives a typical example of fibers tracked with DTI when seeded in the transverse muscle; it can be seen that the majority of the transverse muscle fibers, which should be reconstructed as left to right (red) streamlines, are missing. Therefore, a fiber tracking method that is able to resolve crossing fibers is crucial for correct representation of the tongue muscles.

To address the problem of tracking crossing fibers, different imaging modalities that seek to obtain more comprehensive directional information, including high angular resolution diffusion imaging (HARDI) [15] and diffusion spectrum imaging (DSI) [16], have been proposed. Since these modalities typically acquire around 100 gradient directions and demand long scan times (which limits their application in clinical research), a number of attempts to accelerate the imaging process have been made [17–19]. However, because of the involuntary swallowing, which limits the available time to around 2–3 minutes for *in vivo* acquisition in the tongue, especially in cases where pathology is present, only a dozen (or so) gradient directions are achievable in practice. Thus, there is insufficient time for the acquisition of HARDI and DSI, despite the efforts to accelerate image acquisition. In addition, a great number of existing DTI data sets have been acquired and need better analysis. Therefore, although both HARDI and DSI data could be used for the methods

described in this paper, we limit the presentation of results to the conventional DTI acquisitions that are presently achievable.

There are also methods designed to better exploit the information in DTI to resolve crossing fibers. For example, Behrens et al. [20] and Peled et al. [21] use two-tensor models to recover crossing directions. In Behrens et al. [20], a Bayesian estimation is used to fit the parameters of the model, which is achieved by Markov chain Monte Carlo sampling. The method in Peled et al. [21] places a number of constraints on the tensors in the two-tensor model to reduce the number of free parameters, and resolves two crossing fiber directions using a nonlinear least squares method. Ramirez-Manzanares et al. [22], Landman et al. [23], and Zhou et al. [24] use multi-tensor models with a fixed tensor basis to resolve crossing fibers. In Ramirez-Manzanares et al. [22], diffusion signals are modeled as a discrete mixture of Gaussian random variables and are deconvolved using a set of diffusion basis functions which represent fiber directions. In Landman et al. [23], a sparse reconstruction technique is used, where a dictionary is constructed with a fixed tensor basis. The fiber directions are estimated by solving the ℓ_1 -norm regularized least squares problem. Zhou et al. [24] adds an isotropic component in the multi-tensor model and solves the problem with ℓ_1 -norm and TV-norm regularization.

Using the number of gradient directions that is common in clinical research (around 30), these two-tensor or multi-tensor models are able to resolve crossing fibers. However, due to the limited number of gradient directions in *in vivo* tongue diffusion data acquisition, there is insufficient information for successful resolution of crossing fibers using these methods. Figure 1(b) gives an example of fibers tracked using the multi-tensor model in Landman et al. [23], when the fibers were seeded in the transverse muscle. Although part of the transverse muscle is reconstructed, it is clear that the major body is missing. Thus, distinguishing interdigitated tongue muscles, which constitute a large percentage of the tongue volume, is very challenging.

In this paper, we present a multi-tensor method for distinguishing interdigitated tongue muscles by incorporating prior directional knowledge within a Bayesian framework. The proposed method is named Fiber Interdigitation Estimation by Bayesian Reconstruction (FIEBR). In FIEBR, the prior directional knowledge provides information on likely fiber directions at each voxel, and can be computed with anatomical knowledge of tongue muscles. Note that this work is an extension of our conference paper [25]. Compared to Ye et al. [25], here we have included more comprehensive muscle information and we also propose a way to determine the parameters of the algorithm. In addition, while only one control subject was included in Ye et al. [25], here we have included both control subjects and patients after glossectomies to show the influence of surgeries on the muscles and demonstrate the potential of applying FIEBR for clinical use.

An example of the FIEBR result is shown in Figure 1(c). In contrast to the DTI model and the multi-tensor results in Figures 1(a) and 1(b), FIEBR successfully reconstructs the transverse muscle. In FIEBR, we use a fixed tensor basis to model the diffusion weighted signals in each voxel, and then we determine the contribution of each basis tensor using maximum a posteriori (MAP) estimation. The prior distribution contains both the prior

directional information and sparsity constraints, and data fidelity is modeled in the likelihood term. The resulting objective function can be solved as a noise-aware version of a weighted ℓ_1 -norm minimization [26]. Using the estimated fiber directions from FIEBR, we also propose a streamlining fiber tracking strategy to reconstruct tongue muscles.

The remainder of the paper is organized as follows. Section 2 describes the proposed algorithm. In Section 3, validations of FIEBR are presented on a digital crossing phantom and *in vivo* tongue diffusion data. A discussion is provided in Section 4 and Section 5 summarizes and concludes the paper.

2. Methods

In this section, we first introduce a multi-tensor model with a fixed tensor basis. Then, the MAP estimation of the fiber directions incorporating prior directional knowledge is presented, and an approach to obtaining prior knowledge of tongue muscle fiber directions is provided. A streamlining fiber tracking strategy using the estimated fiber directions is also described. Finally, the constants used in the proposed FIEBR and streamlining algorithms are summarized.

2.1. Multi-tensor Model with a Fixed Tensor Basis

We define a fixed tensor basis comprising N prolate tensors \mathbf{D}_i whose primary eigenvectors (PEVs) are oriented over the sphere. Each \mathbf{D}_i represents a fiber direction given by its PEV. In this work, $N = 253$, the second and third eigenvalues of each basis tensor are equal to $0.5 \times 10^{-3} \text{ mm}^2/\text{s}$, and the primary eigenvalue is equal to $2 \times 10^{-3} \text{ mm}^2/\text{s}$. These eigenvalues are empirically determined by examining the diffusion tensors in regions of noncrossing fiber tracts [23]. At each voxel, the diffusion weighted signals can be modeled as a mixture of the attenuated signals from these tensors. Using the Stejskal-Tanner tensor formulation [27], we have [23]

$$S_k = S_0 \sum_{i=1}^N f_i e^{-b \mathbf{g}_k^T \mathbf{D}_i \mathbf{g}_k} + n_k, \quad (1)$$

where b is the b -value, \mathbf{g}_k is the k -th gradient direction ($k \in \{1, 2, \dots, K\}$ where K is the number of gradient directions), S_k is the diffusion signal in the k -th direction, S_0 is the baseline signal without diffusion weighting, f_i is the (unknown) nonnegative mixture fraction for \mathbf{D}_i , and n_k is a noise term. Note that in this signal model, as in Ramirez-Manzanares et al. [22], Daducci et al. [28], and Landman et al. [23], we do not explicitly

require $\sum_{i=1}^N f_i = 1$, but the f_i 's can be interpreted as mixture fractions when they are normalized to sum to one [23]. By defining $y_k = S_k/S_0$ and $\eta_k = n_k/S_0$, Eq. (1) can be written as:

$$\mathbf{y} = \mathbf{G} \mathbf{f} + \boldsymbol{\eta}, \quad (2)$$

where $\mathbf{y} = (y_1, y_2, \dots, y_K)^T$, \mathbf{G} is a $K \times N$ matrix comprising the attenuation terms $G_{ki} = e^{-b\mathbf{g}_k^T \mathbf{D}_i \mathbf{g}_k}$, $\mathbf{f} = (f_1, f_2, \dots, f_n)^T$, and $\boldsymbol{\eta} = (\eta_1, \eta_2, \dots, \eta_k)^T$.

2.2. Mixture Fraction Estimation with Prior Knowledge

We use MAP estimation to estimate the mixture fractions \mathbf{f} . Accordingly, we seek to maximize the posterior probability of \mathbf{f} given the observations \mathbf{y} . The posterior probability is given by

$$p(\mathbf{f}|\mathbf{y}) = \frac{p(\mathbf{f})p(\mathbf{y}|\mathbf{f})}{\int p(\mathbf{f})p(\mathbf{y}|\mathbf{f})d\mathbf{f}}. \quad (3)$$

Therefore, since the denominator in Eq. (3) is constant with respect to \mathbf{f} , the desired solution is

$$\hat{\mathbf{f}} = \arg \max_{\mathbf{f}} p(\mathbf{f})p(\mathbf{y}|\mathbf{f}) \quad (4)$$

Since at each voxel the number of fiber directions is expected to be small, we promote sparseness in \mathbf{f} by using the Laplace prior density: $p(\mathbf{f}) \propto e^{-\lambda\|\mathbf{f}\|_1}$, where λ is a positive constant. However, sparsity alone is not sufficient prior information when the observations do not include a large number of gradient directions (as in DTI of the *in vivo* tongue). Therefore, we further supplement the prior knowledge with directional information. Suppose prior information about likely fiber directions were known at each voxel. For each voxel, let the prior directions be represented by the collection of vectors $\{\mathbf{w}_1, \mathbf{w}_2, \dots, \mathbf{w}_P\}$, where P is the number of prior fiber directions. A similarity vector \mathbf{a} can be constructed between the directions represented by the basis tensors and the prior directions:

$$\mathbf{a} = (\max_m |\mathbf{v}_1 \cdot \mathbf{w}_m|, \max_m |\mathbf{v}_2 \cdot \mathbf{w}_m|, \dots, \max_m |\mathbf{v}_N \cdot \mathbf{w}_m|)^T, \quad (5)$$

where \mathbf{v}_i is the PEV of the basis tensor \mathbf{D}_i . Each entry a_i in \mathbf{a} represents the similarity between the basis direction \mathbf{v}_i and its closest prior direction. Note that \mathbf{w}_m and \mathbf{v}_i are unit vectors and thus $a_i \in [0, 1]$. We modify the prior density by incorporating the similarity vector as follows: $p(\mathbf{f}) \propto e^{-\lambda\|\mathbf{f}\|_1} e^{\gamma \mathbf{a} \cdot \mathbf{f}}$, where γ is a nonnegative constant. In this way, basis tensors closer to the prior directions are made to be more likely *a priori* (except when $\gamma = 0$ and no prior information is incorporated).

Since $\mathbf{f} \geq \mathbf{0}$, we have

$$\lambda\|\mathbf{f}\|_1 - \gamma \mathbf{a} \cdot \mathbf{f} = \lambda \mathbf{1} \cdot \mathbf{f} - \gamma \mathbf{a} \cdot \mathbf{f} = \lambda \left(\mathbf{1} - \frac{\gamma}{\lambda} \mathbf{a} \right) \cdot \mathbf{f} = \lambda (\mathbf{1} - \alpha \mathbf{a}) \cdot \mathbf{f} = \lambda \|\mathbf{C}\mathbf{f}\|_1, \quad (6)$$

Where

$$\alpha = \frac{\gamma}{\lambda} \quad (7)$$

and \mathbf{C} is a diagonal matrix with $C_{ii} = (1 - \alpha a_i)$ (note that $a_i > 0$). Therefore, $p(\mathbf{f})$ has a truncated Laplace density given by

$$p(\mathbf{f}) = \frac{1}{Z_p(\alpha, \lambda)} e^{-\lambda \|\mathbf{C}\mathbf{f}\|_1}, \quad \mathbf{f} \geq \mathbf{0}, \quad (8)$$

where $Z_p(\alpha, \lambda)$ is a normalization constant. We require $\alpha < 1$ to ensure that $C_{ii} > 0$. Thus, $0 < \alpha < 1$.

Suppose the noise $\boldsymbol{\eta}$ in Eq. (2) follows a Rician distribution. A Rician distribution can be approximated by a Gaussian distribution when the signal to noise ratio is above 3:1 [29], which holds for most observed data in the proposed application. The conditional density for the observed data is then modeled as a Gaussian density: $p(\mathbf{y}|\mathbf{f}) \propto e^{-\|\mathbf{G}\mathbf{f} - \mathbf{y}\|_2^2 / \sigma_\eta^2}$, where σ_η is the noise scale.

Using Eq. (3), we can then write the posterior density as

$$p(\mathbf{f}|\mathbf{y}) = \frac{1}{Z(\alpha, \lambda, \sigma_\eta, \mathbf{G})} e^{-(\|\mathbf{G}\mathbf{f} - \mathbf{y}\|_2^2 / \sigma_\eta^2 + \lambda \|\mathbf{C}\mathbf{f}\|_1)}, \quad (9)$$

where $Z(\alpha, \lambda, \sigma_\eta, \mathbf{G})$ is a normalization constant. The MAP estimate of \mathbf{f} is found by maximizing $p(\mathbf{f}|\mathbf{y})$ or $\ln p(\mathbf{f}|\mathbf{y})$:

$$\hat{\mathbf{f}} = \arg \min_{\mathbf{f} \geq \mathbf{0}} \frac{1}{\sigma_\eta^2} \|\mathbf{G}\mathbf{f} - \mathbf{y}\|_2^2 + \lambda \|\mathbf{C}\mathbf{f}\|_1. \quad (10)$$

By using $\beta = \lambda \sigma_\eta^2$, the minimization in Eq. (10) is equivalent to

$$\hat{\mathbf{f}} = \arg \min_{\mathbf{f} \geq \mathbf{0}} \|\mathbf{G}\mathbf{f} - \mathbf{y}\|_2^2 + \beta \|\mathbf{C}\mathbf{f}\|_1, \quad (11)$$

which is a noise-aware version of a weighted ℓ_1 -norm minimization [26]. We note that this formulation is equivalent to the CFARI objective function developed in Landman et al. [23] when $\alpha = 0$ (i.e., $\mathbf{C} = \mathbf{I}$). Thus, our approach, developed with an alternative Bayesian perspective, is a generalization of the CFARI algorithm.

To solve Eq. (11), we use a new variable $\mathbf{g} = \mathbf{C}\mathbf{f}$. Since \mathbf{C} is diagonal and $C_{ii} > 0$, \mathbf{C} is invertible and therefore $\mathbf{f} = \mathbf{C}^{-1} \mathbf{g}$. Letting $\mathbf{G} = \mathbf{G}\mathbf{C}^{-1}$, we have

$$\hat{\mathbf{g}} = \arg \min_{\mathbf{g} \geq 0} \|\tilde{\mathbf{C}}\mathbf{g} - \mathbf{y}\|_2^2 + \beta \|\mathbf{g}\|_1. \quad (12)$$

We find $\hat{\mathbf{g}}$ using the optimization method in Kim et al. [30] and the mixture fractions \mathbf{f} can be estimated as:

$$\hat{\mathbf{f}} = \mathbf{C}^{-1} \hat{\mathbf{g}}. \quad (13)$$

Finally, the mixture fractions are normalized so that they sum to one:

$$\tilde{f}_i = \frac{\hat{f}_i}{\sum_{j=1}^N \hat{f}_j}. \quad (14)$$

Directions associated with nonzero mixture fractions are interpreted as fiber directions, and the value of f_i indicates the contribution of the corresponding direction in the diffusion signal.

2.3. Prior Directions for the Tongue Muscles

To obtain prior directions, we built a template by manually identifying regions of interest (ROIs) for the genioglossus (GG), the geniohyoid (GH), the inferior longitudinal muscle (IL), the superior longitudinal muscle (SL), the transverse muscle (T), and the vertical muscle (V) according to Takemoto [31] on a high resolution structural image (0.8 mm isotropic) of a subject. Examples of these identified muscles on the template are shown in Figure 2. T interdigitates with GG near the mid-sagittal planes and with V on lateral parts of the tongue. GG and V intersect with SL near the top and back surface of the tongue. The interdigitation of the tongue muscles is summarized in Table 1.

The b_0 image (the image without diffusion weighting) was also acquired for this template subject in the same position as the high resolution structural image. A mask of the tongue area was delineated on the b_0 image. The muscle ROIs were subsampled to have the same resolution as the b_0 image. For each test subject, a manual mask of the tongue was drawn on the b_0 image. We used SyN deformable registration [32] between the b_0 images masked by the tongue regions to deform the template to the target space, where cross correlation was used as the similarity metric.

Using deformed ROIs of the tracts, the prior directions can be obtained as follows. GG is known to be fan-shaped; therefore, we use fan-shaped prior directions for GG, as illustrated in Figure 3(a). Specifically, the origin of GG in the mid-sagittal slice can be identified on the test subject during the delineation of the whole tongue. Suppose the x -axis represents the left-right (L-R) direction, the y -axis represents the anterior-posterior (A-P) direction, and the z -axis represents the inferior-superior (I-S) direction. Then at a voxel $\mathbf{x}_{\text{GG}} = (x_{\text{GG}}, y_{\text{GG}}, z_{\text{GG}})$ belonging to GG, fanning GG prior directions can be obtained with respect to the GG origin (x_0, y_0, z_0) as

$$\mathbf{w}_{GG} = (0, y_{GG} - y_0, z_{GG} - z_0). \quad (15)$$

Similarly, since V is known to fan out like GG, for a voxel $\mathbf{x}_V = (x_V, y_V, z_V)$ in V, its prior fiber direction is set as

$$\mathbf{w}_v = (0, y_V - y_0, z_V - z_0). \quad (16)$$

The GH and IL have A-P fiber directions, therefore in GH and IL voxels we use

$$\mathbf{w}_{GH} = \mathbf{w}_{IL} = (0, 1, 0) \quad (17)$$

as the prior directions. The fibers in T propagate transversely, therefore the prior direction \mathbf{w}_T of a T voxel is

$$\mathbf{w}_T = (1, 0, 0). \quad (18)$$

Finally, SL has arc-shaped fibers close to the top and back surface of the tongue, as illustrated in Figure 3(a). The approximate circle center for the arc in the mid-sagittal slice is manually identified on the test subject as $\mathbf{x}_c = (x_c, y_c, z_c)$. For a voxel $\mathbf{x}_{SL} = (x_{SL}, y_{SL}, z_{SL})$ belonging to SL, its prior direction can be calculated as

$$\mathbf{w}_{SL} = (0, -(z_{SL} - z_c), y_{SL} - y_c), \quad (19)$$

which is tangential to the arc. An example of the prior directions on a test subject is shown in Figure 3(b). The directions are color-coded by the standard DTI scheme. Note that in the coronal view, the A-P directions (GH and IL) are not visible, and in the sagittal view, the L-R directions (T) are not visible.

It is possible that the prescribed knowledge is incorrect due to an anatomical abnormality or error in its specification. Some variation is to be expected and can be compensated by selecting the weight assigned to the prior knowledge appropriately (see experiments below). However, when the prior knowledge varies grossly from the data, it is best to recognize this and adaptively downweight or remove this particular prior knowledge. For example, when there is one fiber direction ($P = 1$), the priors should not deviate much from that fiber direction; when there are two fiber directions ($P = 2$), the prior directions should be close to the plane defined by the two fiber directions, or in other words they are close to orthogonal to the normal of the plane.

One way of removing incorrect priors is to use the diffusion tensor information, which is calculated from the diffusion weighted images (DWIs). Suppose the first and third eigenvectors of the diffusion tensor are \mathbf{v}_{d1} and \mathbf{v}_{d3} , respectively; \mathbf{v}_{d1} provides an estimate of the fiber direction when there is no crossing fiber, and \mathbf{v}_{d3} provides an estimate of the normal of the plane defined by the fiber directions when there are two crossing fibers. Accordingly, we discard prior fiber directions when

$$\arccos|\mathbf{w}_1 \cdot \mathbf{v}_{d1}| > \xi_1, \text{ if } P=1 \quad (20)$$

Or

$$\min_{m=\{1,2\}} \arccos|\mathbf{w}_m \cdot \mathbf{v}_{d3}| < \xi_2, \text{ if } P=2, \quad (21)$$

where ξ_1 and ξ_2 are thresholds.

2.4. Fiber Tracking

Given the FIEBR estimated fiber directions, fiber tracking can be carried out using a streamlining technique similar to Landman et al. [23]. Starting from a seed voxel, the fiber directions with $f_i > t_{mf}$ are used to initiate fibers, where t_{mf} is a threshold, because directions with small f_i 's are interpreted as components of isotropic diffusion. For each initiated fiber, at each step, one of the fiber directions in the current voxel is selected as the propagation direction until the fiber reaches the next voxel. In selecting fiber directions, only those with $f_i > t_{mf}$ are considered. As in Landman et al. [23], the fiber direction that maximizes the importance weighting $f_i |\mathbf{v}_i \cdot \mathbf{v}_{last}|^4$ is selected. Here \mathbf{v}_{last} is the unit propagation direction in the previous tracking step. Starting and terminating criteria based on fractional anisotropy (FA) are used. Only voxels with FA larger than a threshold t_{FA} are used to initiate fibers, and when fibers reach FA values lower than t_{FA} , they are terminated. Finally, a turning angle threshold θ_t is used: when the angle between the current and previous propagation directions is larger than θ_t , the fibers are terminated. In this work, $t_{mf} = 0.1$, $t_{FA} = 0.2$, and $\theta_t = 40^\circ$, which are common settings in other DTI fiber tracking algorithms [23, 33, 34].

2.5. Summary of Constants

A table summarizing the constants used in the proposed method is shown in Table 2. α , β , ξ_1 , and ξ_2 are used in the mixture fraction estimation, and t_{mf} , t_{FA} , and θ_t are used in the fiber tracking process. Note that for α and β , different values are used based on the levels of noise. Their values are determined in Section 3.1.3 and are not listed in Table 2.

3. Results

FIEBR was first applied on a digital crossing phantom. Different settings of α and β (see Eqs. (7) and (11)) were tested with different levels of noise. In addition, we studied the influence of the accuracy of prior knowledge. Parameters learned from these computational phantom studies were used on the next set of experiments involving *in vivo* tongue diffusion data, where three control subjects and four patients with glossectomies were included. Fiber directions were estimated and muscle fibers were tracked on all seven subjects. These results are visualized for qualitative comparison and histograms of fiber directions are numerically evaluated for quantitative comparison.

3.1. Digital Crossing Phantom

A 3D crossing phantom with two tracts crossing at 90° was generated to verify the operation of the FIEBR algorithm. A two-tensor model is used for the generation of the simulated

diffusion signals [35]. Figure 4 shows an axial view of this computational phantom. Twelve diffusion gradient direction acquisitions (with $b = 500 \text{ s/mm}^2$) were simulated and both FIEBR and CFARI [23] were applied to these data. The eigenvalues of the basis tensors were determined as described in Section 2.1 and they were also used for the phantom generation.

3.1.1. Noise-free Case—First we applied FIEBR on this noise-free phantom for a proof-of-concept experiment. The horizontal and vertical directions—i.e., the correct directions—were used as the prior directions for the horizontal and vertical tracts, respectively. A result with $\alpha = 0.5$ and $\beta = 0.05$ is shown and compared with CFARI results ($\beta = 0.05$) in Figures 4(a) and 4(b). Here the standard DTI color scheme is used. Since directions with small \tilde{f}_i 's are interpreted as components of isotropic diffusion, we only show directions with $\tilde{f}_i > t_{\text{mf}}$. In the crossing regions, CFARI fails to produce the correct crossing directions (Figure 4(a)), while FIEBR correctly generates the crossing pattern (Figure 4(b)).

Next, we studied the performance of FIEBR with inaccurate prior directions. To introduce errors in the prior directions, we rotated the true directions by $\theta = 10^\circ$ and used the rotated directions as the prior directions. Two cases of rotations were tested: in and out of the axial plane. Specifically, in the first case the horizontal and vertical directions were both rotated clockwise in the axial plane; and in the second case the horizontal directions were rotated around the vertical line out of the axial plane and the vertical directions were rotated around the horizontal line out of the axial plane. The results of the two cases are shown in Figures 4(c) and 4(d). In both cases, even with inaccurate prior directions, FIEBR correctly estimates noncrossing and crossing fiber directions.

3.1.2. Influence of Noise, Algorithm Parameters, and Prior Direction

Inaccuracies—To make the simulation more realistic, we added Rician noise in the phantom test. We selected three sample voxels in the phantom: one in the noncrossing horizontal tract, one in the noncrossing vertical tract, and one in the crossing region. Different levels of Rician noise η in Eq. (2) were added to the sample voxels. We describe the noise level using the signal-to-noise ratio (SNR) S_0/σ_η where S_0 is the b_0 image intensity and σ_η is the scale of the Rician noise distribution. We also tested with different values of α , β , and prior direction inaccuracy θ . The inaccurate prior directions were obtained with in-plane and out-of-plane rotation by θ . The sets of the testing parameters were: $S_0/\sigma_\eta \in \Sigma_\eta = \{+\infty, 25, 12.5, 8.33\}$, $\alpha \in A = \{0.1, 0.2, \dots, 0.9, 0.99\}$, $\beta \in B = \{0.05, 0.2, 0.4, \dots, 2.0\}$, and $\theta \in \Theta = \{0^\circ, 10^\circ, 20^\circ, 30^\circ\}$. For each combination of S_0/σ_η , α , β , and θ , 100 simulations were performed for each sample voxel.

To quantitatively evaluate the results, we define two error measures for angles:

$$e_1 = \frac{1}{N_1} \sum_{\substack{i=1 \\ \tilde{f}_i > t}}^N \min_j \arccos(\mathbf{v}_i \cdot \mathbf{u}_j) \cdot \frac{180^\circ}{\pi}, \quad (22)$$

$$e_2 = \frac{1}{N_2} \sum_{j=1}^{N_2} \min_{i: \tilde{f}_i > t} \arccos(\mathbf{v}_i \cdot \mathbf{u}_j) \cdot \frac{180^\circ}{\pi}. \quad (23)$$

Here N_1 is the number of directions with normalized mixture fractions \tilde{f}_i larger than a threshold t (in this case $t = 0.1$), \mathbf{v}_i is the basis direction, \mathbf{u}_j is the ground truth of fiber directions, and N_2 is the number of ground truth directions. N_2 can be 1 or 2, depending on whether fiber crossing exists at the location. e_1 measures how close the estimated directions are to the ground truth, and e_2 measures how well each true direction is estimated. Note that using only e_1 or e_2 is insufficient because the estimated directions can agree with one of the true crossing directions and ignore the other, or each true direction can be properly estimated but there are other estimated directions representing incorrect directions.

Examples of the mean errors of the estimated fiber directions are plotted in Figures 5 and 6 for $S_0/\sigma_\eta = 25$, $\theta \in \{0^\circ, 10^\circ\}$, $\alpha \in A$, and $\beta \in B$. For the inaccurate prior directions rotated by θ , the results of the in-plane and out-of-plane cases are averaged. The results for the two noncrossing voxels are averaged as the noncrossing cases. Note that the cases with $\alpha = 0$ are equivalent to CFARI results.

Figure 5 shows examples when noise of $S_0/\sigma_\eta = 25$ is added to noncrossing voxels. Using the correct prior directions ($\theta = 0^\circ$) reduces the effect of noise (see Figures 5(a) and 5(c)). When errors are introduced in the prior directions, the effect of noise can still be reduced with the proper selection of α and β (see $\alpha = 0.4$ and $\beta = 1.2$ in Figures 5(b) and 5(d)). Figure 6 gives examples of the crossing cases. It can be seen that the effect of noise can be reduced with true or inaccurate prior directions. Note that for $\theta = 10^\circ$, the errors can be smaller than 10° , which indicates the result is better than simply using the prior directions as the estimate.

3.1.3. Determination of Algorithm Parameters Based on Noise Levels—We used all the combinations of S_0/σ_η , α , β , and θ to determine the best parameter settings for real data. For each combination of S_0/σ_η , α , and β , we averaged the errors with different θ for the noncrossing and crossing cases separately. Then for each S_0/σ_η , the α and β which minimize the average error using all the θ were selected for the noncrossing and crossing cases. Using the plots in Figures 5 and 6 and other similar plots not shown, the selection is summarized in Table 3. This table is later used to determine α and β in the real data application.

Based on Table 3, different α and β values are used for different levels of noise. To calculate S_0/σ_η we first estimate the image noise scale σ_η by placing a bounding box in the background. Here we assume the background noise follows a Rayleigh distribution, and σ_η^2 can be estimated as [36]

$$\hat{\sigma}_\eta^2 \approx \frac{1}{2N_b} \sum_{i=1}^{N_b} I_i^2, \quad (24)$$

where I_i 's are the intensities of the background voxels in the bounding box, and N_b is the number of these voxels. Then, σ_η is estimated as

$$\hat{\sigma}_\eta \approx \sqrt{\hat{\sigma}_\eta^2}. \quad (25)$$

Thus, at each voxel x , using the estimated noise scale $\hat{\sigma}_\eta$, the b_0 image intensity $S_0(x)$, and Table 3, we decide $\alpha(x)$ and $\beta(x)$ as follows. In noncrossing regions:

$$(\alpha(x), \beta(x)) = \begin{cases} (0.5, 0.2), & \text{if } S_0(x)/\hat{\sigma}_\eta > 50 \\ (0.4, 0.6), & \text{if } 16.67 < S_0(x)/\hat{\sigma}_\eta \leq 50 \\ (0.5, 1.0), & \text{if } 10 < S_0(x)/\hat{\sigma}_\eta \leq 16.67 \\ (0.5, 1.6), & \text{if } S_0(x)/\hat{\sigma}_\eta \leq 10 \end{cases} \quad (26)$$

In crossing regions:

$$(\alpha(x), \beta(x)) = \begin{cases} (0.5, 0.2), & \text{if } S_0(x)/\hat{\sigma}_\eta > 50 \\ (0.7, 0.6), & \text{if } 16.67 < S_0(x)/\hat{\sigma}_\eta \leq 50 \\ (0.8, 1.0), & \text{if } 10 < S_0(x)/\hat{\sigma}_\eta \leq 16.67 \\ (0.6, 1.6), & \text{if } S_0(x)/\hat{\sigma}_\eta \leq 10 \end{cases} \quad (27)$$

In this way, the selected parameter pairs minimize the average errors at their corresponding noise levels.

3.2. In Vivo Tongue Diffusion Data

Experiments were then performed on *in vivo* tongue diffusion data, where three control subjects and four patients with glossectomies were included. DWIs were acquired on a 3T MR scanner (Magnetom Trio, Siemens Medical Solutions, Erlangen, Germany). Each scan has 12 gradient directions and one b_0 image. The b -value is 500 s/mm². The field of view (FOV) is 240 mm × 240 mm × 84 mm. TR/TE=5000/68 ms. The resolution is 3 mm isotropic. The acquisition of each subject took about two minutes and 30 seconds, which must be this short because the involuntary urge to swallow occurs about every two minutes. We applied FIEBR on the subjects using the parameter settings in Eqs. (26) and (27), which are computed independently for each voxel. The eigenvalues of the basis tensors were set as described in Section 2.1. For each subject, the FIEBR processing took around 10 minutes.

3.2.1. Application to Control Subjects—An example of the estimated fiber directions on a representative control subject is shown and compared with the PEV of the diffusion tensor and the CFARI algorithm [23] in Figure 7. In the mid-sagittal view, we highlight the regions of GG crossing with SL, and in the mid-coronal view, a region of GG/V and T crossing is highlighted. The PEV alone obviously cannot represent crossing fiber directions and the CFARI algorithm fails to resolve crossing fibers, while FIEBR is able to recover the crossing directions.

In Figure 8, we plot the distribution of fiber directions in the whole tongue of this control subject for all three algorithms. The distributions are plotted on the upper part of the unit sphere and viewed from top. The surface of the hemisphere is divided into bins by discretizing the azimuth angle and the elevation angle. In each bin, the density is calculated by dividing the number of the fiber directions that fall in the bin by the bin area. In the FIEBR result, there are many L-R fiber directions, which are indicated by the bins near $(-1, 0)$ and $(1, 0)$ (highlighted as region A in Figure 8(c)). The L-R directions represent the T fiber directions. There are also many fiber directions in the A-P direction, which are indicated by the bin near $(0, -1)$ (highlighted as region B in Figure 8(c)). These directions represent the IL, GH, and part of GG fibers. The three bins on the negative part of the line $x = 0$ show the fanning pattern of GG fiber directions (highlighted as region C in Figure 8(c)). In the results from the PEVs and CFARI, far fewer L-R directions are observed.

Next, fiber tracking was performed for further validation of the fiber direction estimation. Using fiber tracking, we can evaluate the coherence of the fiber directions qualitatively. We placed seeds in GG and T separately. The results on the representative control subject are shown in Figures 9 and 10, where FIEBR is compared with both the FACT algorithm [11] and the fiber tracking method proposed in Landman et al. [23] that uses CFARI results. The visualization of fibers was created in TrackVis [37], where the fibers are color-coded by the orientation of each segment.

In Figure 9, it can be seen that many of the GG fibers produced by FACT and CFARI terminate due to the crossing of GG with T and SL, while FIEBR tracks GG through these crossing regions (see the highlighted region). It is also evident that FIEBR produces smoother and more fan-shaped GG fibers than FACT and CFARI. Note that because of the seeds placed in crossing regions, in the FIEBR result we can also observe that some T and SL fibers are tracked. In Figure 10, FACT fails to produce T fibers, and CFARI only produces T fibers at the anterior portion of the tongue, while FIEBR reconstructs transverse T fibers throughout the tongue.

3.2.2. Application to Patients with Glossectomies—We now show FIEBR results when applied to patients with glossectomies. An example and comparison of fiber tracking results is shown in Figure 11. Here we show the areas that are affected by the surgery near the mid-sagittal plane. Seeds were placed in GG. Compared to FACT and CFARI, FIEBR tracks GG through the crossing areas of GG and T (see the highlighted region). In the FIEBR result, it can be seen that sparser GG fibers in the lesion were tracked than outside the lesion. Note that because of seeding in the crossing regions of GG and T, some T fibers were also produced in the FIEBR result, and the T fibers are also sparser in the lesion than outside the lesion.

3.2.3. Comparison between Controls and Patients with Glossectomies—To investigate the influence of glossectomies on the muscles, we computed fiber direction histograms for all patients. The distributions of the fiber directions in the tongue are plotted in Figure 12. Compared with the distribution in Figure 8, patients 1, 3, and 4 show a similar organization of fiber directions, while patient 2 has a very different fiber organization. To quantitatively demonstrate this, we calculated the symmetric Kullback–Leibler divergence

for the direction distributions between the subjects and list the result in Table 4. It can be seen that the divergence values between patient 2 and other subjects are much larger than those between the other subject pairs. We also notice that patient 4 has a pattern that appears to be more similar to those of patients 1 and 3 than those of the control subjects.

4. Discussion

There is insufficient information for the CFARI algorithm to correctly resolve crossing fibers given DTI acquisitions with only 12 gradient directions. This is because there can be multiple solutions with the sparsity regularization alone and the output fiber directions can simply be dependent on the implementation of the optimization algorithm. Therefore, we further add prior directional information in the estimation problem to account for the insufficient information.

In the crossing phantom test, we observed that the inclusion of prior directional information enables the method to find the crossing patterns and reduce the effect of noise, even with inaccurate prior directions. The choice of the parameters should consider the factors such as noise levels and prior direction inaccuracy. Because the noise level can be estimated from the image but it is difficult to determine how accurate the prior information is, we tested different prior direction inaccuracies for each noise level, and used the average performance to decide the parameter setting for the real data application. These settings achieved results that are consistent with the anatomical structures of the muscles. For example, we have tracked transverse T fibers and fanning GG fibers.

In the experiments on real tongue data, FIEBR tracks crossing fibers better than FACT [11] with the single tensor model and CFARI [23] which usually requires around 30 gradient directions. The addition of prior knowledge can also have a smoothing effect on fiber tracking. For the patients, the method is still able to distinguish interdigitated muscles, such as GG and T. It also reflects the anomalies caused by glossectomies, where the GG and T fibers terminate in the lesion.

The case study between the subjects shows that the control subjects share a consistent pattern of fiber directions (indicated by the divergence values in Table 4). Less organized fiber directions were observed in patient 2 while the other three patients have similar fiber direction distributions to the control subjects. This could indicate that patient 2 is more affected by the glossectomy, where tongue muscles must be adapted to function after the surgery. We also observed that patient 4 is more similar to patients 1 and 3 than to the controls, which is consistent with the fact that patient 1, 3, and 4 all underwent glossectomies. This case study provides a possible example of applying the proposed method for clinical use.

Segmentation of the muscles is currently obtained by registration of a template. It provides general locations of the muscles but it is possible that mis-registration can happen at the boundaries. Therefore, before using the prior knowledge, we inspect the agreement between the prior directions and the diffusion information as shown in Eqs. (20) and (21) to reduce the influence of inaccurate prior directions. In the future, the registration could be replaced by a carefully designed volumetric segmentation algorithm to improve the segmentation

accuracy. In the brain, such algorithms have been developed—e.g., Bazin et al. [38], Ye et al. [39], and Yendiki et al. [40]. There is also an effort that segments the *ex vivo* calf tongue muscles [3]. These methods could be adapted and then applied on the human tongue muscles to provide better ROIs of muscles.

Unlike the major brain white matter tracts, the geometries of the tongue muscles are relatively simple and their fiber directions do not have large variability. This anatomical simplicity allows us to compute prior directions and use them for reconstructing tongue muscles. It is also possible to apply the FIEBR algorithm to other simple structures such as the mylohyoid muscle and the palatopharyngeus muscle. For complex structures like white matter tracts, specification of prior directions is not straightforward and would need further investigation.

5. Summary and Conclusion

In this work, we have proposed a Bayesian approach to distinguishing interdigitated tongue muscles with limited diffusion magnetic resonance imaging by incorporating prior directional knowledge. The diffusion weighted signals are modeled with a fixed tensor basis. We use MAP estimation, where the prior directional information and the sparsity of the basis tensors are included in the prior distribution, and data fidelity is ensured in the likelihood term. The fiber directions are estimated by solving the resulting weighted ℓ_1 -norm regularized least squares problem. Using the estimated fiber directions, a fiber tracking method is also presented.

The method was first applied on a digital crossing phantom for quantitative evaluation, and the results show that the use of prior information can correctly resolve crossing fibers and reduce the effect of noise. Based on the phantom results, parameter settings were determined for real data. Then the experiments were performed on *in vivo* tongue diffusion data and the results demonstrate that the proposed method is able to resolve crossing tongue muscle fibers with limited gradient directions. A case study on three control subjects and four patients with glossectomies shows that the method can reveal the difference in fiber direction distributions between subjects. In particular, the Kullback–Leibler divergence values indicate that one of the patients is observed to have quite different organizations of fiber directions than the other subjects. This case study provides a potential tool to examine the influence of glossectomies on tongue muscles.

Acknowledgments

This work is supported by NIH/NINDS 1R21NS082891, NIH/NCI 5R01CA133015, NIH/NINDS 5R01NS056307, and the China Scholarship Council.

References

1. Lowe AA, Sessle BJ. Tongue activity during respiration, jaw opening, and swallowing in cat. *Canadian Journal of Physiology and Pharmacology*. 1973; 51:1009–1011. [PubMed: 4591134]
2. Hiiemae KM, Palmer JB. Tongue movements in feeding and speech. *Critical Reviews in Oral Biology & Medicine*. 2003; 14:413–429. [PubMed: 14656897]

3. Kim S, Barnett A, Pierpaoli C, Chi-Fishman G. Three-dimensional mapping of lingual myoarchitecture by diffusion tensor MRI. *NMR in Biomedicine*. 2008; 21:479–488. [PubMed: 17952877]
4. Gilbert RJ. Three-dimensional muscular architecture of the human tongue determined in vivo with diffusion tensor magnetic resonance imaging. *Dysphagia*. 2005; 20:1–7. [PubMed: 15886960]
5. Gaige T, Benner T, Wang R, Wedeen V, Gilbert R. Three dimensional myoarchitecture of the human tongue determined in vivo by diffusion tensor imaging with tractography. *Journal of Magnetic Resonance Imaging*. 2007; 26:654–661. [PubMed: 17685446]
6. Felton SM, Gaige TA, Benner T, Wang R, Reese TG, Wedeen VJ, Gilbert RJ. Associating the mesoscale fiber organization of the tongue with local strain rate during swallowing. *Journal of Biomechanics*. 2008; 41:1782–1789. [PubMed: 18456271]
7. Murano EZ, Shinagawa H, Zhuo J, Gullapalli RP, Ord RA, Prince JL, Stone M. Application of diffusion tensor imaging after glossectomy. *Otolaryngology–Head and Neck Surgery*. 2010; 143:304–306. [PubMed: 20647140]
8. Shinagawa H, Murano E, Zhuo J, Landman B, Gullapalli R, Prince J, Stone M. Effect of oral appliances on genioglossus muscle tonicity seen with diffusion tensor imaging: A pilot study. *Oral Surgery, Oral Medicine, Oral Pathology, Oral Radiology, and Endodontology*. 2009; 107:e57–e63.
9. Shinagawa H, Murano EZ, Zhuo J, Landman B, Gullapalli RP, Prince JL, Stone M. Tongue muscle fiber tracking during rest and tongue protrusion with oral appliances: A preliminary study with diffusion tensor imaging. *Acoustical Science and Technology*. 2008; 29:291–294.
10. Basser PJ, Mattiello J, LeBihan D. MR diffusion tensor spectroscopy and imaging. *Biophysical Journal*. 1994; 66:259–267. [PubMed: 8130344]
11. Mori S, Crain BJ, Chacko V, Van Zijl P. Three-dimensional tracking of axonal projections in the brain by magnetic resonance imaging. *Annals of Neurology*. 1999; 45:265–269. [PubMed: 9989633]
12. Lazar M, Weinstein D, Tsuruda J, Hasan K, Arfanakis K, Meyerand M, Badie B, Rowley H, Haughton V, Field A, Alexander A. White matter tractography using diffusion tensor deflection. *Human Brain Mapping*. 2003; 18:306–321. [PubMed: 12632468]
13. Weinstein D, Kindlmann G, Lundberg E. Tensorlines: Advection-diffusion based propagation through diffusion tensor fields. *Proceedings of the conference on Visualization'99: celebrating ten years*, IEEE Computer Society Press. :249–253.
14. Wiegell MR, Larsson HB, Wedeen VJ. Fiber crossing in human brain depicted with diffusion tensor MR imaging. *Radiology*. 2000; 217:897–903. [PubMed: 11110960]
15. Tuch DS, Reese TG, Wiegell MR, Makris N, Belliveau JW, Wedeen VJ. High angular resolution diffusion imaging reveals intravoxel white matter fiber heterogeneity. *Magnetic Resonance in Medicine*. 2002; 48:577–582. [PubMed: 12353272]
16. Wedeen VJ, Hagmann P, Tseng WYI, Reese TG, Weisskoff RM. Mapping complex tissue architecture with diffusion spectrum magnetic resonance imaging. *Magnetic Resonance in Medicine*. 2005; 54:1377–1386. [PubMed: 16247738]
17. Merlet, S.; Caruyer, E.; Deriche, R. *Medical Image Computing and Computer-Assisted Intervention–MICCAI 2012*. Springer; 2012. Parametric dictionary learning for modeling EAP and ODF in diffusion MRI; p. 10-17.
18. Gramfort, A.; Poupon, C.; Descoteaux, M. *Medical Image Computing and Computer-Assisted Intervention–MICCAI 2012*. Springer; 2012. Sparse DSI: Learning DSI structure for denoising and fast imaging; p. 288-296.
19. Bilgic B, Setsompop K, Cohen-Adad J, Yendiki A, Wald LL, Adalsteinsson E. Accelerated diffusion spectrum imaging with compressed sensing using adaptive dictionaries. *Magnetic Resonance in Medicine*. 2012; 68:1747–1754. [PubMed: 23008145]
20. Behrens TEJ, Berg HJ, Jbabdi S, Rushworth MFS, Woolrich MW. Probabilistic diffusion tractography with multiple fibre orientations: What can we gain? *NeuroImage*. 2007; 34:144–155. [PubMed: 17070705]
21. Peled S, Friman O, Jolesz F, Westin CF. Geometrically constrained two-tensor model for crossing tracts in DWI. *Magnetic Resonance Imaging*. 2006; 24:1263–1270. [PubMed: 17071347]

22. Ramirez-Manzanares A, Rivera M, Vemuri BC, Carney P, Mareci T. Diffusion basis functions decomposition for estimating white matter intravoxel fiber geometry. *IEEE Transactions on Medical Imaging*. 2007; 26:1091–1102. [PubMed: 17695129]
23. Landman BA, Bogovic JA, Wan H, ElShahaby FEZ, Bazin PL, Prince JL. Resolution of crossing fibers with constrained compressed sensing using diffusion tensor MRI. *NeuroImage*. 2012; 59:2175–2186. [PubMed: 22019877]
24. Zhou Q, Michailovich O, Rathi Y. Resolving complex fibre architecture by means of sparse spherical deconvolution in the presence of isotropic diffusion. *SPIE Medical Imaging, International Society for Optics and Photonics*. :903425–903425.
25. Ye, C.; Carass, A.; Murano, E.; Stone, M.; Prince, JL. Bayesian and graphical Models for Biomedical Imaging. Vol. 8677. Springer; 2014. A Bayesian approach to distinguishing interdigitated muscles in the tongue from limited diffusion weighted imaging; p. 13-24. *Lecture Notes in Computer Science*
26. Candes EJ, Wakin MB, Boyd SP. Enhancing sparsity by reweighted ℓ_1 minimization. *Journal of Fourier Analysis and Applications*. 2008; 14:877–905.
27. Stejskal EO, Tanner JE. Spin diffusion measurements: spin echoes in the presence of a time-dependent field gradient. *The Journal of Chemical Physics*. 1965; 42:288.
28. Daducci A, Van De Ville D, Thiran JP, Wiaux Y. Sparse regularization for fiber ODF reconstruction: From the sub optimality of ℓ_1 and ℓ_2 priors to ℓ_0 . *Medical Image Analysis*. 2014; 18:820–833. [PubMed: 24593935]
29. Gudbjartsson H, Patz S. The Rician distribution of noisy MRI data. *Magnetic Resonance in Medicine*. 1995; 34:910–914. [PubMed: 8598820]
30. Kim SJ, Koh K, Lustig M, Boyd S. An efficient method for compressed sensing. *IEEE International Conference on Image Processing*. 3:117–120.
31. Takemoto H. Morphological analyses of the human tongue musculature for three-dimensional modeling. *Journal of Speech, Language, and Hearing Research*. 2001; 44:95–107.
32. Avants BB, Epstein CL, Grossman M, Gee JC. Symmetric diffeomorphic image registration with cross-correlation: evaluating automated labeling of elderly and neurodegenerative brain. *Medical Image Analysis*. 2008; 12:26–41. [PubMed: 17659998]
33. Thomas C, Humphreys K, Jung KJ, Minshew N, Behrmann M. The anatomy of the callosal and visual-association pathways in high-functioning autism: A DTI tractography study. *Cortex*. 2011; 47:863–873. [PubMed: 20832784]
34. Wu EX, Wu Y, Nicholls JM, Wang J, Liao S, Zhu S, Lau CP, Tse HF. MR diffusion tensor imaging study of post infarct myocardium structural remodeling in a porcine model. *Magnetic Resonance in Medicine*. 2007; 58:687–695. [PubMed: 17899595]
35. Ye C, Bazin PL, Ying SH, Prince JL. A fiber tracking method guided by volumetric tract segmentation. *2012 IEEE Workshop on Mathematical Methods in Biomedical Image Analysis (MMBIA)*. :137–142.
36. Sijbers J, den Dekker A, Audekerke JV, Verhoye M, Dyck DV. Estimation of the noise in magnitude MR images. *Magnetic Resonance Imaging*. 1998; 16:87–90. [PubMed: 9436952]
37. Wang R, Benner T, Sorensen AG, Wedeen VJ. Diffusion toolkit: a software package for diffusion imaging data processing and tractography. *Proc Intl Soc Mag Reson Med*. 15:3720.
38. Bazin PL, Ye C, Bogovic JA, Shiee N, Reich DS, Prince JL, Pham DL. Direct segmentation of the major white matter tracts in diffusion tensor images. *NeuroImage*. 2011; 58:458–468. [PubMed: 21718790]
39. Ye C, Yang Z, Ying SH, Prince JL. Segmentation of the cerebellar peduncles using a random forest classifier and a multi-object geometric deformable model: Application to spinocerebellar ataxia type 6. *Neuroinformatics*. 2015:1–15. [PubMed: 25326433]
40. Yendiki A, Panneck P, Srinivasan P, Stevens A, Zoöllei L, Augustinack J, Wang R, Salat D, Ehrlich S, Behrens T, Jbabdi S, Gollub R, Fischl B. Automated probabilistic reconstruction of white-matter pathways in health and disease using an atlas of the underlying anatomy. *Frontiers in Neuroinformatics*. 2011; 5

Highlights (for review)

- We resolve crossing tongue muscles with limited diffusion gradient directions.
- We use prior direction knowledge and formulate the problem in an MAP framework.
- Fiber directions are estimated using a noise-aware weighted L1-norm minimization.
- The method reduces the effect of noise and resolves crossing fibers.
- The method was applied on patients to show its potential for clinical use.

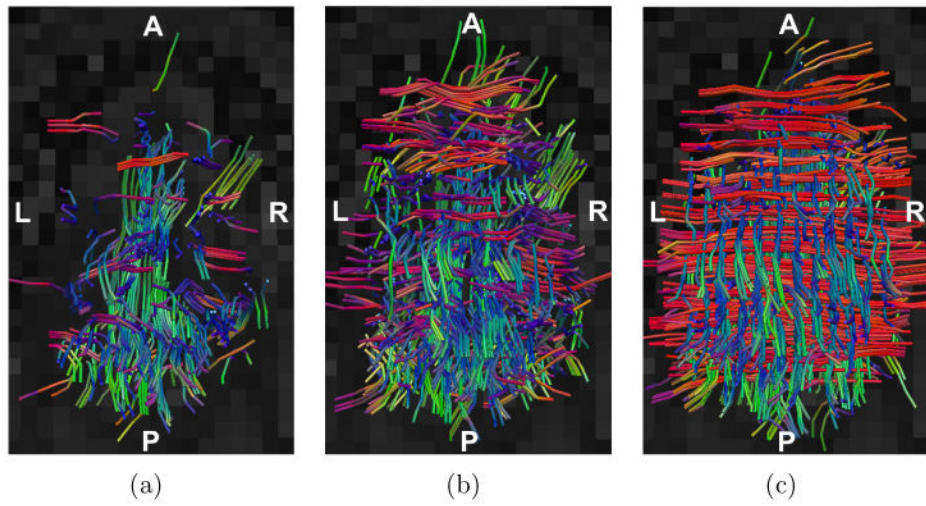


Figure 1.

An example of fiber tracking seeded in the transverse muscle, which in this axial view should be seen as left to right (red) streamlines. Each segment of the fibers is color-coded by the standard DTI color scheme (red: left-right; green: front-back; and blue: up-down). (a) DTI model. (b) Multi-tensor model. (c) Proposed method with prior information.

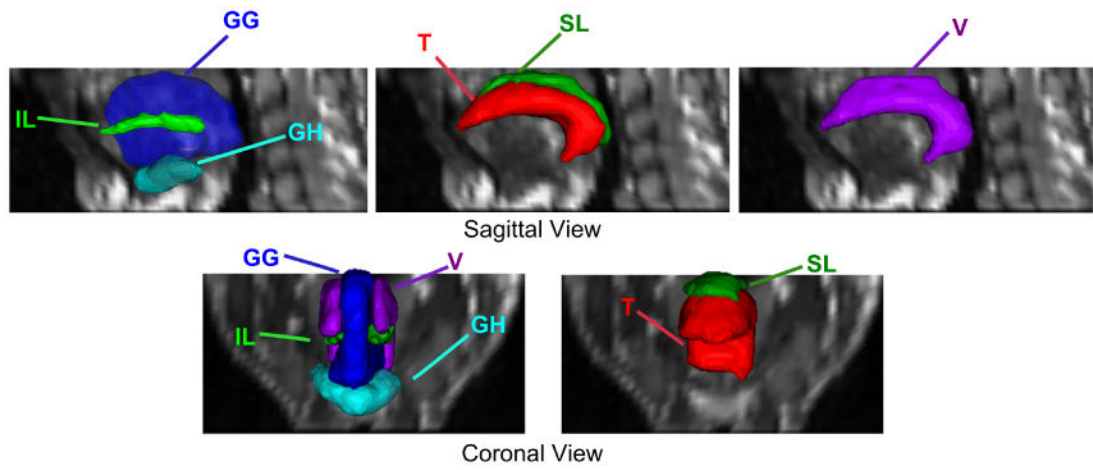


Figure 2. The muscles on the template in the sagittal view and coronal view. Note that muscles shown together are not overlapping.

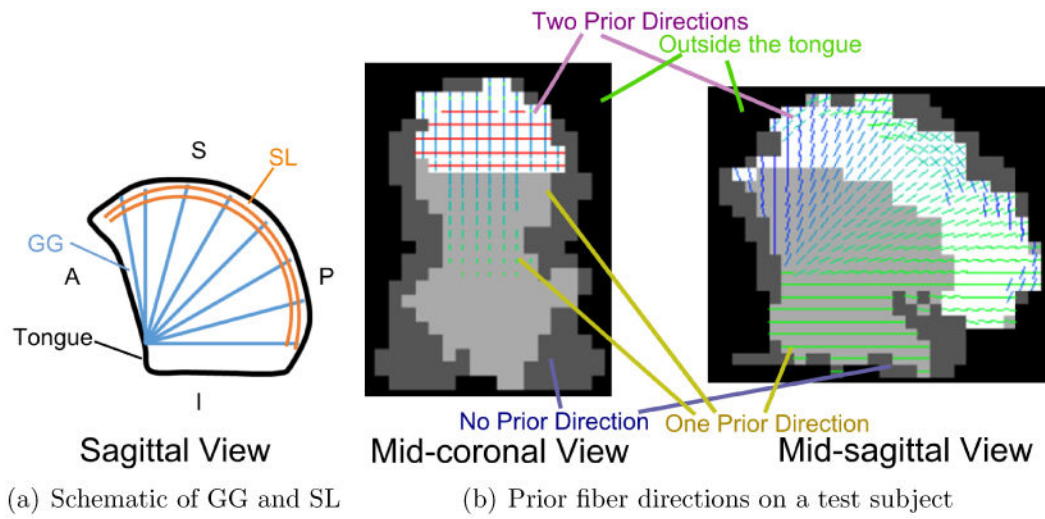


Figure 3.

(a) A schematic of GG and SL fiber directions (sagittal view). (b) An example of prior fiber directions on a test subject in the mid-coronal view and mid-sagittal view. The directions are color-coded by the standard DTI scheme. Note that in the coronal view, A-P directions (GH and IL) are not visible, and in the sagittal view, L-R directions (T) are not visible.

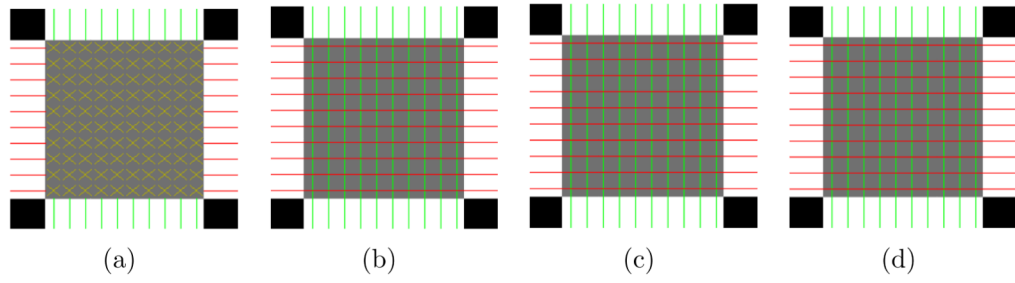


Figure 4. Axial view of the FA of the crossing phantom. Estimated fiber directions from (a) CFARI and (b)-(d) FIEBR when (b) the prior directions are correct, (c) the prior directions are rotated by 10° in the plane, and (d) the prior directions are rotated by 10° out of the plane.

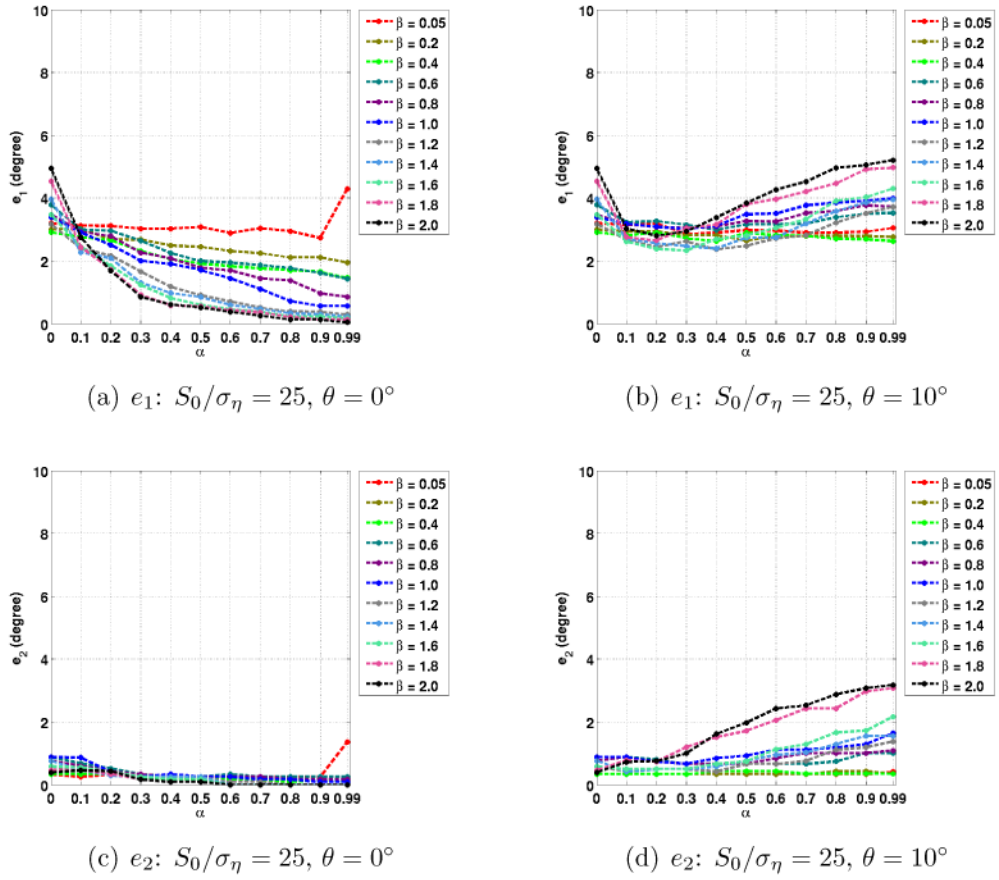


Figure 5. Mean e_1 and e_2 errors in the noncrossing cases with $S_0/\sigma_\eta = 25$ and different θ , α , and β .

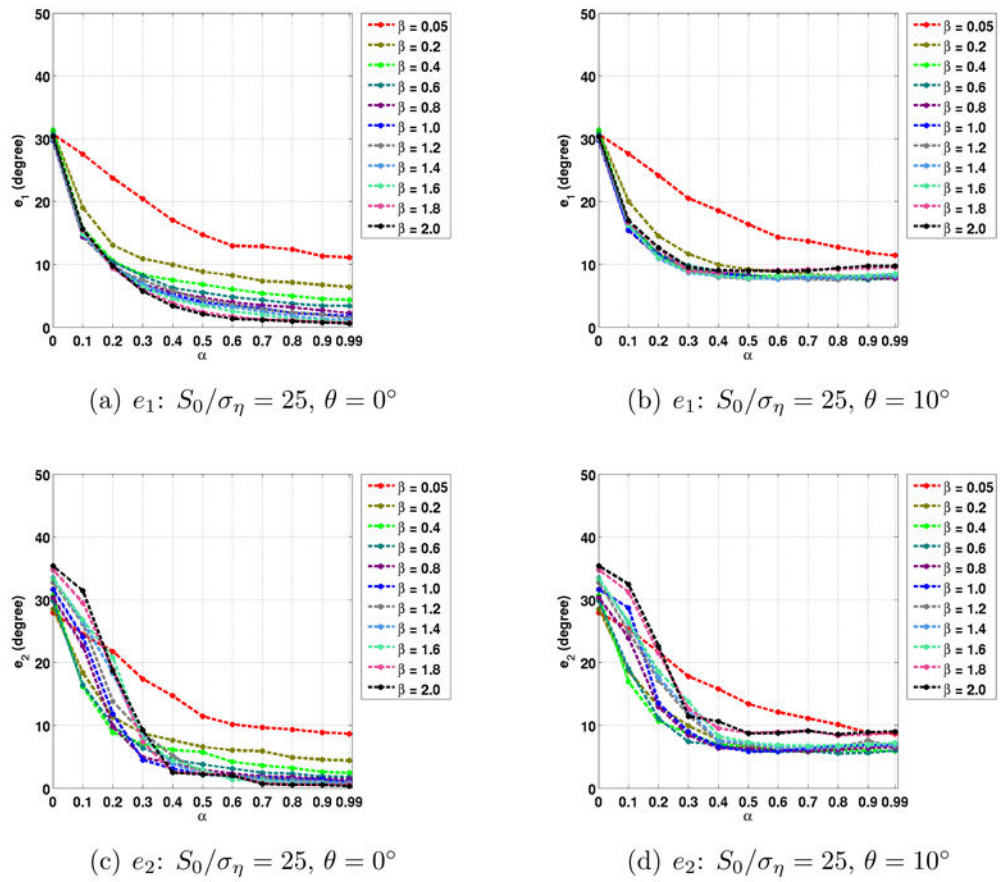


Figure 6. Mean e_1 and e_2 errors in the crossing cases with $S_0/\sigma_\eta=25$ and different θ , α , and β .

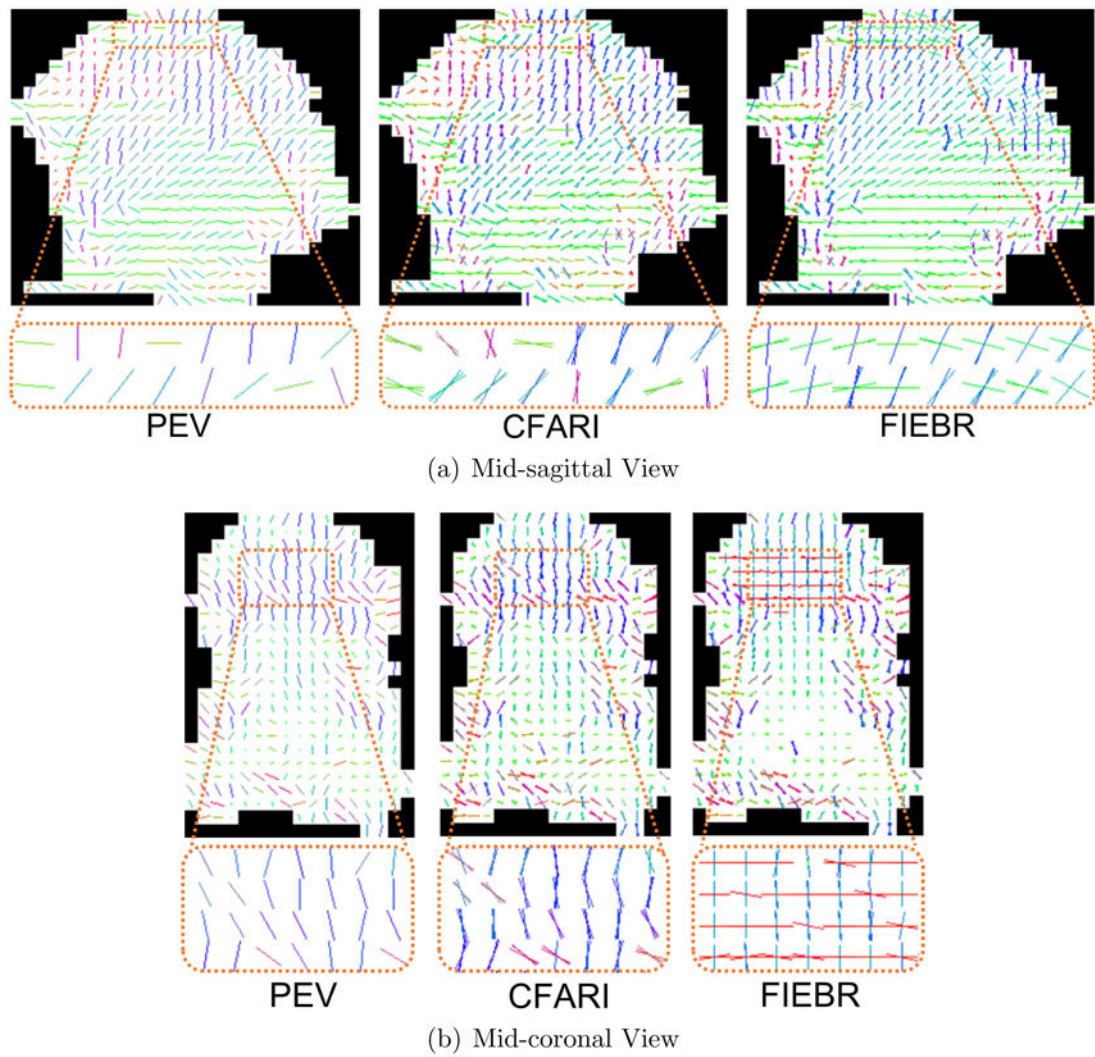


Figure 7. Estimated fiber directions from FIEBR compared with the PEV and the CFARI algorithm: (a) mid-sagittal view and (b) mid-coronal view. Note the highlighted regions for comparison.

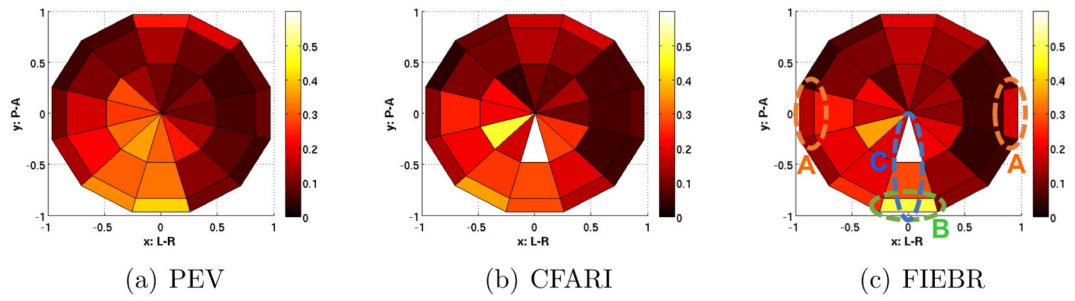


Figure 8.

Distribution of fiber directions of a representative control subject plotted on the upper unit sphere. The hemisphere is viewed from top. Regions are highlighted in the FIEBR result for evaluation.

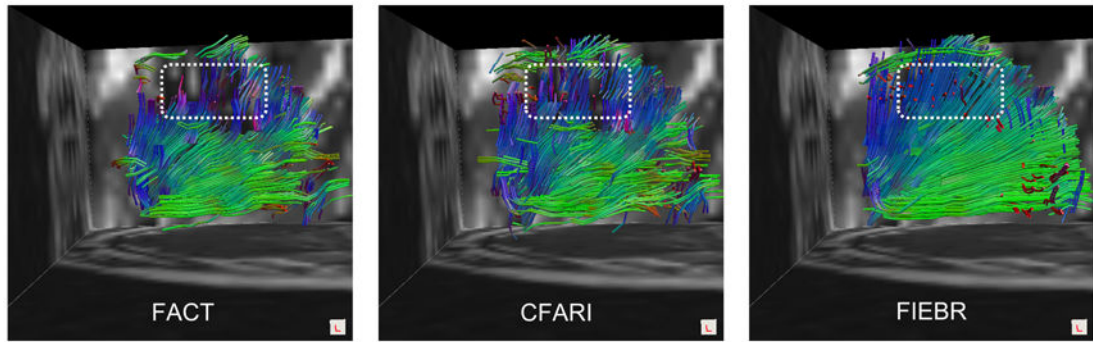


Figure 9.
Fiber tracking results seeded in GG. Note the highlighted region for comparison.

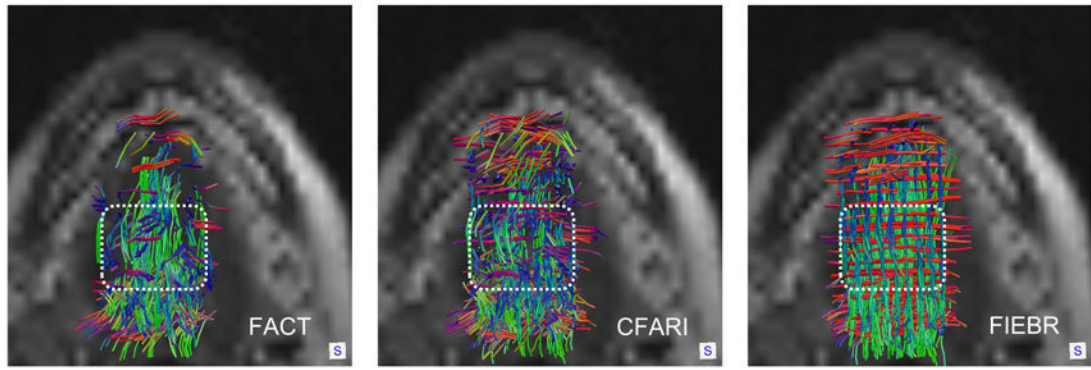


Figure 10. Fiber tracking results seeded in T. Note the highlighted region for comparison.

Author Manuscript

Author Manuscript

Author Manuscript

Author Manuscript

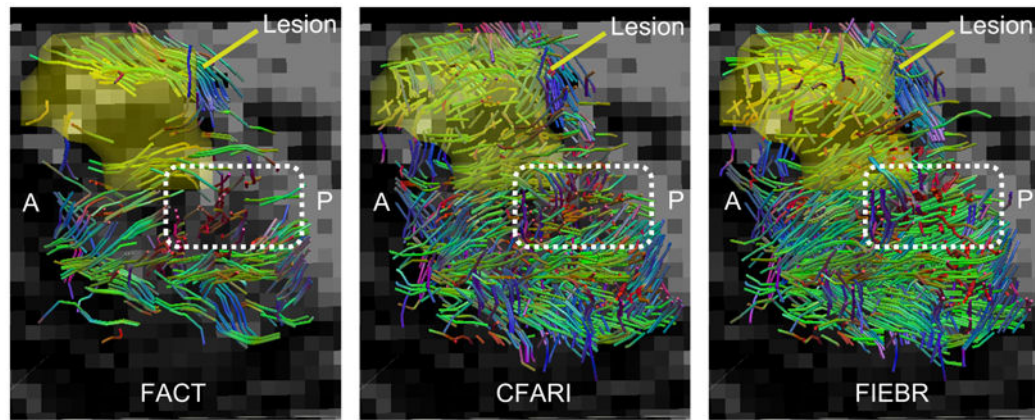


Figure 11.

Fiber tracking results seeded in GG on a patient with a glossectomy. The results are shown near the lesion, which was delineated on the sagittal slices near the mid-sagittal plane. Note the highlighted region for comparison.

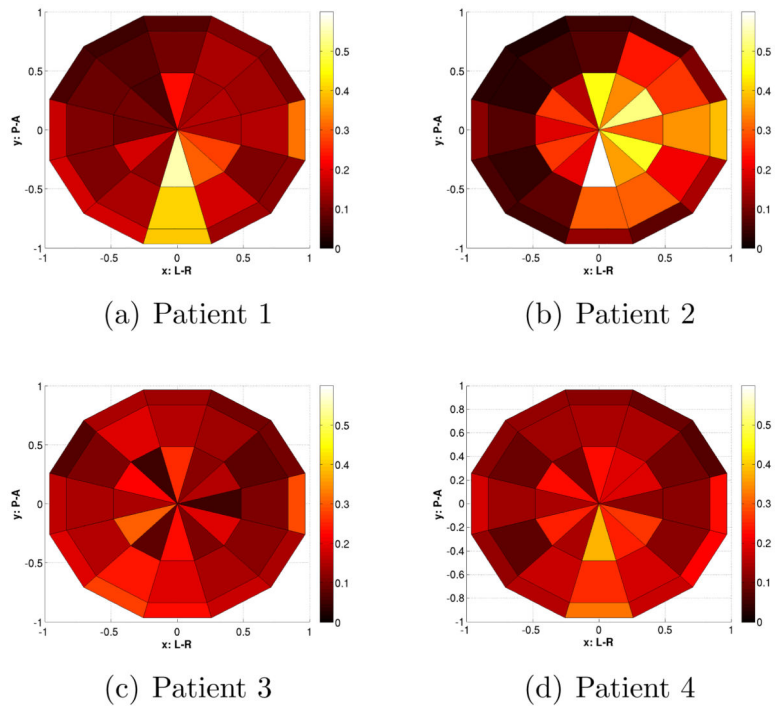


Figure 12. Distributions of fiber directions of the patients plotted on the upper unit sphere. The hemisphere is viewed from top.

Table 1

A summary of interdigitated tongue muscles. Note: “n” and “x” stand for noncrossing and crossing, respectively.

	GG	GH	IL	SL	T	V
GG	n	x	x	x	n	n
GH	n	n	n	n	n	n
IL	n	n	n	n	n	n
SL	x	n	n	n	x	x
T	x	n	n	n	x	x
V	n	n	n	x	x	x

Table 2

A summary of the constants used in the proposed method.

	Constants	Default Values
Mixture Fraction Estimation	α	N/A
	β	N/A
	ξ_1	$\pi/4$
	ξ_2	$\pi/4$
Fiber Tracking	t_{mf}	0.1
	t_{FA}	0.2
	θ_t	40°

Table 3

A summary of the selected α and β with different S_0/σ_H

	Noncrossing Case			Crossing Case				
S_0/σ_H	$+\infty$	25	12.5	8.33	$+\infty$	25	12.5	8.33
α	0.5	0.4	0.5	0.5	0.5	0.7	0.8	0.6
β	0.2	0.6	1.0	1.6	0.2	0.6	1.0	1.6

Table 4

The symmetric Kullback–Leibler divergence of the fiber direction distributions between subjects.

	Control 1	Control 2	Control 3	Patient 1	Patient 2	Patient 3	Patient 4
Control 1	0	0.1292	0.0956	0.1117	0.3886	0.1316	0.1111
Control 2		0	0.1820	0.1356	0.4486	0.1028	0.1086
Control 3			0	0.1266	0.3483	0.1104	0.1255
Patient 1				0	0.1958	0.1279	0.0604
Patient 2					0	0.3541	0.2010
Patient 3						0	0.0594
Patient 4							0